Optics and Lasers in Engineering 148 (2022) 106765

Contents lists available at ScienceDirect

Optics and Lasers in Engineering

journal homepage: www.elsevier.com/locate/optlaseng

# All-fiber-optic LIBS system for tissue differentiation: A prospect for endoscopic smart laser osteotomy

Hamed Abbasi[a,*], Raphael Guzman[b], Philippe C. Cattin[c], Azhar Zam[a,*]

[a] Biomedical Laser and Optics Group (BLOG), Department of Biomedical Engineering, University of Basel, CH-4123 Allschwil, Switzerland
[b] Department of Neurosurgery, University Hospital Basel, CH-4056 Basel, Switzerland
[c] Center for medical Image Analysis and Navigation (CIAN), Department of Biomedical Engineering, University of Basel, CH-4123 Allschwil, Switzerland

ARTICLE INFO

*Keywords:*
FO-LIBS
Miniaturization
High throughput
Echelle spectrometer
Tissue characterization

ABSTRACT

Minimally-invasive laser surgeries could benefit from a fiber-optic laser-induced breakdown spectroscopy (FO-LIBS) setup for real-time tissue characterization. In FO-LIBS, the sample receives limited light irradiance due to the fiber's low damage threshold and diminished laser beam quality. Therefore, the plasma created with FO-LIBS is less luminant than that of free-space LIBS. Furthermore, only a small portion of plasma emission can be collected, as the lens's size at the fiber tip is restricted to fit inside the narrow channel of an endoscope. A high optical throughput Echelle spectrometer was developed to compensate for low-intensity light collection with FO-LIBS. The Echelle spectrometer was tested for tissue differentiation when combined with a flexible fiber bundle delivery setup and a small lens at the bundle's tip. The customized FO-LIBS setup, coupled with multivariate data analysis, successfully differentiated bone from surrounding soft tissue (muscle, fat, and bone marrow) with 100% cross-validated (CV) sensitivity and specificity. The CV sensitivity and specificity for differentiation between all tissues were 90.2% and 96.7%, respectively. The results demonstrate, to the best of our knowledge, the first flexible FO-LIBS system, which may provide a further step towards the development of a smart endoscopic laser scalpel.

## 1. Introduction

Traditional mechanical tools (e.g., saws, drills, chisels) used for bone cutting — the gold standard in osteotomy for thousands of years — require a certain degree of mechanical force (like grinding or hammering) to function [1,2]. The mechanical pressure exerted by saws and drills (contact mode cutting) presents some disadvantages for use as an osteotomy tool, including poor surface evenness, high risk of contamination, substantial material loss, metal abrasion, limited cutting geometry, bone fragmentation, and thermal damage. Moreover, saws and drills can create an amorphous, mineral-rich carbon layer on the bone surface, changing the mineralized matrix, which results in a prolonged healing process [3,4]. Due to the many side effects of using conventional osteotomy tools, alternative solutions are being sought. Some of the lesser-known techniques for osteotomy proposed and examined over the last decades include machining based on microwaves, ion beams, ultrasonic energy, water jets, and lasers [5,6]. Laser beams do not deflect while traveling (unlike water jets) and do not carry momentum. Lasers interact with materials without mechanical interaction forces and thus contactless. Without such mechanical forces, the body movements during surgery are minimized, and consequently, intraoperative image guidance systems can perform with higher accuracy. Several studies have been carried out to compare the performance of laserosteotomy with the conventional mechanical saws and drills as well as piezoelectric cutting tools. Using a laser beam offers a high axial and lateral resolution, allowing for a high degree of freedom when cutting. This freedom provides significant advantages during surgery, particularly oral and maxillofacial surgery, where implants are used to replace parts of the bone. Microstructural analysis, namely micro-computed tomography (CT) and histological examinations, have shown that more new mineralized bone is formed in cuts being performed with a laser rather than a piezo-osteotome (PZE) [7]. Accelerated healing of laserosteotomy is also reported here [8]. Histological and radiological examinations revealed primary gap healing in sheep two months post-laserosteotomy, and almost no visible osteotomy gap after three months [9]. While preoperative planning can navigate the laser to the required area, a lack of real-time monitoring risks iatrogenic damage due to any possible number of unpredicted errors or body movement. Therefore, real-time feedback is vital to preventing damage to the surrounding soft tissues during laserosteotomy. To avoid such damage, several optical approaches have been developed, including laser-induced breakdown spectroscopy (LIBS), laser-induced breakdown thresholding, diffuse reflectance spec-

* Corresponding authors.
*E-mail addresses:* hamed.abbasi@unibas.ch (H. Abbasi), azhar.zam@unibas.ch (A. Zam).

https://doi.org/10.1016/j.optlaseng.2021.106765
Received 19 February 2021; Received in revised form 18 June 2021; Accepted 27 July 2021

troscopy (DRS), Raman spectroscopy, autofluorescence spectroscopy, random lasing, optical coherence tomography (OCT), speckle analysis, shockwave measurement, and combustion/pyrolysis light analysis. A short overview of these feedback methods is provided elsewhere [10]. Of the approaches mentioned above, LIBS is an up-and-coming technique for analyzing biological tissues, especially calcified tissues like bone. It allows for analysis without sample preparation and, with a single shot, reveals the material's chemical composition under the cut in a few milliseconds [11-17]. Multiple studies have shown the potential of using LIBS to differentiate bone from other soft tissues, such as muscle, fat, skin, nerve, mucosa, liver, tendon, as well as cartilage [18-26]. The studies differentiated between the soft tissues surrounding bone, except for bone marrow. Moreover, none of the studies mentioned could simultaneously fulfill the complete set of requirements for a minimally-invasive laserosteotomy feedback system, including the possibility of insertion inside the narrow channel of a flexible endoscope. A delivery system capable of transmitting tens of megawatts of nanosecond pulses of frequency-doubled Nd:YAG (532 nm) was recently developed [27]. The fiber delivery system developed showed high flexibility and bend-insensitive behavior. Flexibility is of high importance for compatibility with flexible endoscopes. This study aims to develop a method capable of providing optical feedback on the type of tissue being cut, namely bone, bone marrow, muscle, and fat (adipose), using the flexable fiber delivery system and a custom-made sensitive Echelle spectrometer dedicated to this application.

## 2. Materials and methods

While a large body of research on using LIBS for biological tissue analysis exists, most studies utilized free-space beam delivery and fiber-optic light collection [28-35]. In free-space LIBS, sufficient peak power can be delivered to the sample surface by simply using a few mirrors and/or lenses. Moreover, the laser beam maintains focusability, as it does not pass through an optical fiber. Therefore, the beam can be focused onto a relatively small focal spot, allowing for higher irradiance of the sample. Without space limitations, free-space LIBS can use bulky light collectors/collimators to collect more light from the laser-induced plasma. The light collectors/collimators employ wide diameter lenses/mirrors to maximize optical throughput light collection (low F-number). Although this is the most efficient way of performing LIBS analysis, the bulky setup can not be miniaturized for endoscopic applications. Minimally-invasive surgery requires a miniaturized beam delivery setup. In other words, the laser pulse should be delivered to the sample via optical fibers; this limits the amount of deliverable peak power to the sample (due to the limited laser-induced damage threshold (LIDT) of optical fibers) and prevent the use of bulky light collectors/collimators. In such a setup, the plasma emissions cannot be collected with high optical throughput (i.e., the smaller the lens/mirror diameter, the lower the optical throughput). Commercially available Echelle spectrometers typically have a high F-number of 10 or more [36-40], which results in low optical throughput. For this reason, a custom-made Echelle spectrometer was designed and developed with higher optical throughput than those available on the market. For use in minimally-invasive surgery, fiber-optic LIBS (FO-LIBS) must also collect the plasma light using the same fiber employed for laser beam delivery, as space inside the endoscope is limited. For flexible endoscopic applications, the fiber system should be flexible down to a bending radius of approximately 15 mm [41] and operate without bending loss. While a few researchers have used either a fiber laser [21] or a laser coupled to a fiber optic [42,43] for beam delivery during biological tissue analysis with LIBS, none of them achieved the conditions for flexible endoscopic application — namely, a common fiber for both beam delivery and light collection with flexible and bend-insensitive behavior, and small focusing/collection optics at the tip of the fiber.

### 2.1. Fiber-based laser beam delivery

Due to the limited LIDT of glass, large solid-core fiber or hollow-core fiber are typically used for delivering the high peak powers required for LIBS, typically in the gigawatt (GW) range. Using large-core fibers limits the bending radius, which depends on the fiber's core and cladding thickness. Therefore, a high-power delivery setup was recently developed to achieve bend-insensitive flexible beam delivery. The setup uses a beam shaper and a fused-end fiber bundle of 800 individual fibers (CeramOptec GmbH, Bonn, Germany), with low numerical aperture (NA) launch conditions [27]. A single small half-ball lens focuses the laser beam on the sample and collects the plasma emission. Fig. 1 shows the dimensions of the fiber system.

As shown in Fig. 1, the length of the solid parts inside of the endoscope is 13.5 mm; other parts are flexible with a minimum bending radius of 15 mm (tested) [27]. The diameter of the parts inside the endoscope are small enough to fit inside an endoscope with an internal diameter of 10 mm [44]. At the bundle input, the jackets were removed and individual fibers were fused together, providing a solid structure without gaps between the individual fibers. The length and diameter of the fused part of the bundle were 10 mm and 3 mm, respectively. For other parts of the bundle, the jackets of individual fibers were not removed and the individual fibers remained unattached to maintain flexibility. The diameter of the total bundle was 3.5 mm. At the bundle output, individual fibers were glued to each other. The core, cladding, and jacket diameter of individual fibers were 100 µm, 106 µm, and 112 µm, respectively. Fig. 2 shows the input and output bundle facets.

This study used a pulsed Q-switched Nd:YAG laser (Q-smart 450, Quantel, France) working at its fundamental harmonic (1064 nm), with a pulse duration of 6 ns. A green, low-power continuous wave (CW) diode laser, aligned with the pulsed laser beam, was used to visualize the focal spot. A top-hat beam shaper (GTH-5-250-4-532, TOPAG Lasertechnik GmbH, Darmstadt, Germany) was employed to illuminate all individual fibers within the fiber bundle with equal energy. An air nozzle helped to prevent dust from reaching the surface of the fiber bundle. The bundle exhibited bend-insensitive behavior due to using low-order modes to launch the bundle (tested with different bending radiuses down to 1.5 cm). More information about the fiber delivery process can be found elsewhere [27]. Fig. 3 (a) and (b) shows the experimental setup for laser beam delivery and plasma emission collection.

The same optical fiber and half-ball lens used to deliver the laser pulses were used to collect the plasma emission. The surface of the half-ball lens was wiped off with a lens cleaning tissue when needed (to clean the surface from the deposited particle due to tissue ablation). An off-axis parabolic (OAP) mirror with a through-hole (the pierced mirror in Fig. 3) allowed the laser beam to pass through while simultaneously directing the plasma emission to the spectrometer's optical fiber.

### 2.2. Echelle spectrometer

Bandwidth, resolution, and optical throughput are three spectrometer parameters that cannot be maximized simultaneously. Attempts to maximize all parameters at the same time result in either a very bulky setup (not portable and very expensive, like spectrometers designed for observatories), or a spectrometer incapable of snapshot collection (spectrometers with mechanical movable parts), which cannot be used for fast measurements [45]. Two-dimension spectroscopic configurations such as the Echelle designs have helped achieve wider bandwidth without losing resolution. Still, it is not possible to accomplish high-resolution, high-throughput, and wide bandwidth at the same time. Therefore, parameters were optimized according to the application.

The sensitivity of a spectrometer is a function of its optical throughput. The optical throughput, i.e. how much light can pass through the spectrometer, is indicated by its F-number; the lower the F-number, the higher the throughput. High F-numbers can reduce the sensitivity of the spectrometer. The plasma plume created with FO-LIBS is less luminant

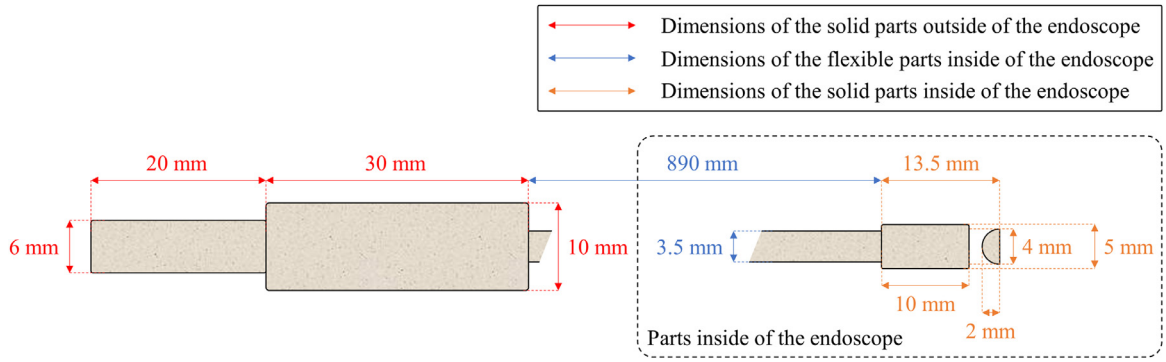


**Fig. 1.** Dimensions of the developed fiber system (input from the left side, the output from the right side) in relation to endoscopic placement. The half-ball lens shown on the right was used to focus the laser beam and collect the plasma emission simultaneously.

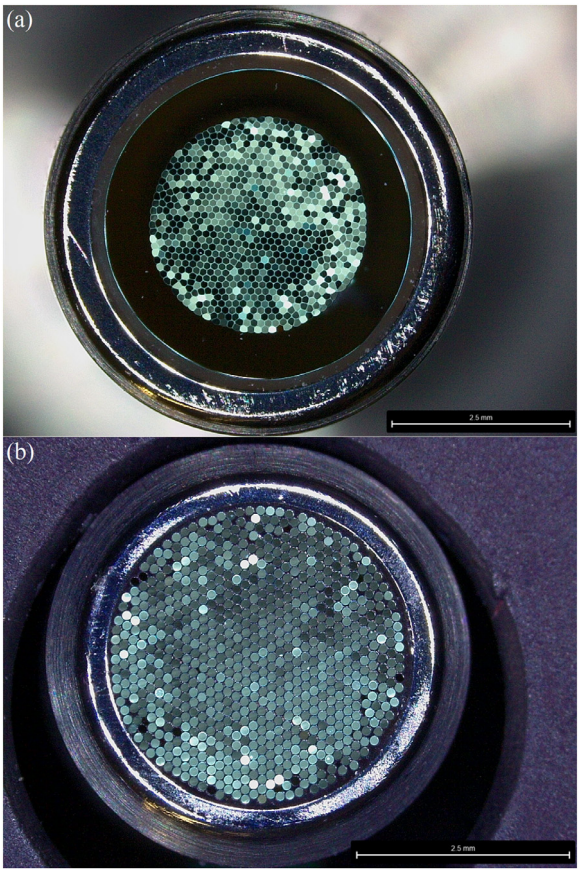


**Fig. 2.** (a) Input, and (b) output facets of the bundle. The images were captured using a digital microscope (Leica DVM6, Leica Microsystems GmbH, Germany). The scale shown is 2.5 mm in both (a) and (b).

(due to limited deliverable energy and reduced focusability) than that created with free-space LIBS. This fact, along with the small portion of plasma light collected by the small lens at the fiber tip, results in the spectrometer receiving low-intensity light. Therefore, a custom-made Echelle spectrometer was developed to compensate for low throughput light collection. The spectrometer was developed by simulating the mechanical and optical parts in Solidworks, Matlab, and Zemax (OpticStudio) [46], to find the most suitable components and to provide better performance than the previously developed Echelle spectrometer by the authors [45]. Fig. 4 shows the experimental setup of the customized Echelle spectrometer.

Light fed by an optical fiber patch cord (NA=0.12, core diameter=50 μm, acting as input slit) inside the spectrometer travels from the fiber output to the first OPA mirror (with an effective focal length (EFL) of 152.4 mm). After reflecting off of the mirror's surface, the collimated light reaches the Echelle grating in a quasi-Littrow orientation. A Littrow configuration would cause the center of each diffracted order to reflect back exactly on its path, thereby returning the light to the fiber. By tilting the Echelle grating from its initial position (quasi-Littrow configuration), the fiber no longer poses an obstacle to the beam. There are several ways of inducing this kind of off-axis angle in the system. The Echelle grating can be tilted either around its grooves (perpendicular to the optical table) or around the diffraction orientation (perpendicular to grooves). The former displaces the beam laterally, while the latter shifts the beam vertically. Unlike lateral displacement, vertical displacement is the same for all diffracted orders. If displacement is the same for all wavelengths in the interval of the Echellogram, then any defocusing can be corrected by simply adjusting the imaging lens. However, different displacements result in a curved imaging plane that cannot be adjusted easily unless additional optics are used. Another way to induce vertical displacement is to tilt the Echelle grating around its surface normal. Downside vertical displacement is not helpful as it directs the light to the fiber's holder (optical post and post holder). Therefore, the Echelle grating was tilted around its surface normal in a way that yielded an upside displacement. The tilt angle can be determined by gradually tilting the grating until the beam is no longer blocked by the fiber. The beam is collimated by a second OPA mirror with the same EFL as the first OPA mirror, after passing above the fiber. The second OPA mirror was installed in an antiparallel configuration to cancel out the aberration caused by the first one [47]. Both OPA mirrors have an off-axis angle of 90°; this angle was chosen based on its availability on the market. However, a mirror with a lower off-axis angle (e.g., 30°), which was not commercially available through optics catalogs at the time of development, might slightly diminish the aberration [47]. The collimated beam reflected from the second OPA mirror's surface is directed toward a cross-disperser to separate the overlapping Echelle orders. A blazed ruled grating was used here as the cross-disperser. The grooves in the cross-disperser grating were perpendicular to those of the Echelle grating. After the cross-disperser, similar to the beam's situation after being diffracted from the Echelle grating, an off-axis angle is needed to allow the beam to reach the imaging lens without obstruction from the second OPA mirror. The degree of tilt required here is higher than that of the Echelle grating to overcome the larger obstruction of the OPA mirror (compared to the smaller fiber obstruction). A high optical density (OD) longpass filter was used to filter half of the beam's cross-section diffracted from the cross-disperser (also known as ordered sorting). The separated orders are directed to the imaging lens to form the Echellogram on the camera's pixels. The optical base plate is $90 \times 60\ cm^2$. The size of the setup without the camera is (l)44 cm × (w)36 cm × (h)13 cm.

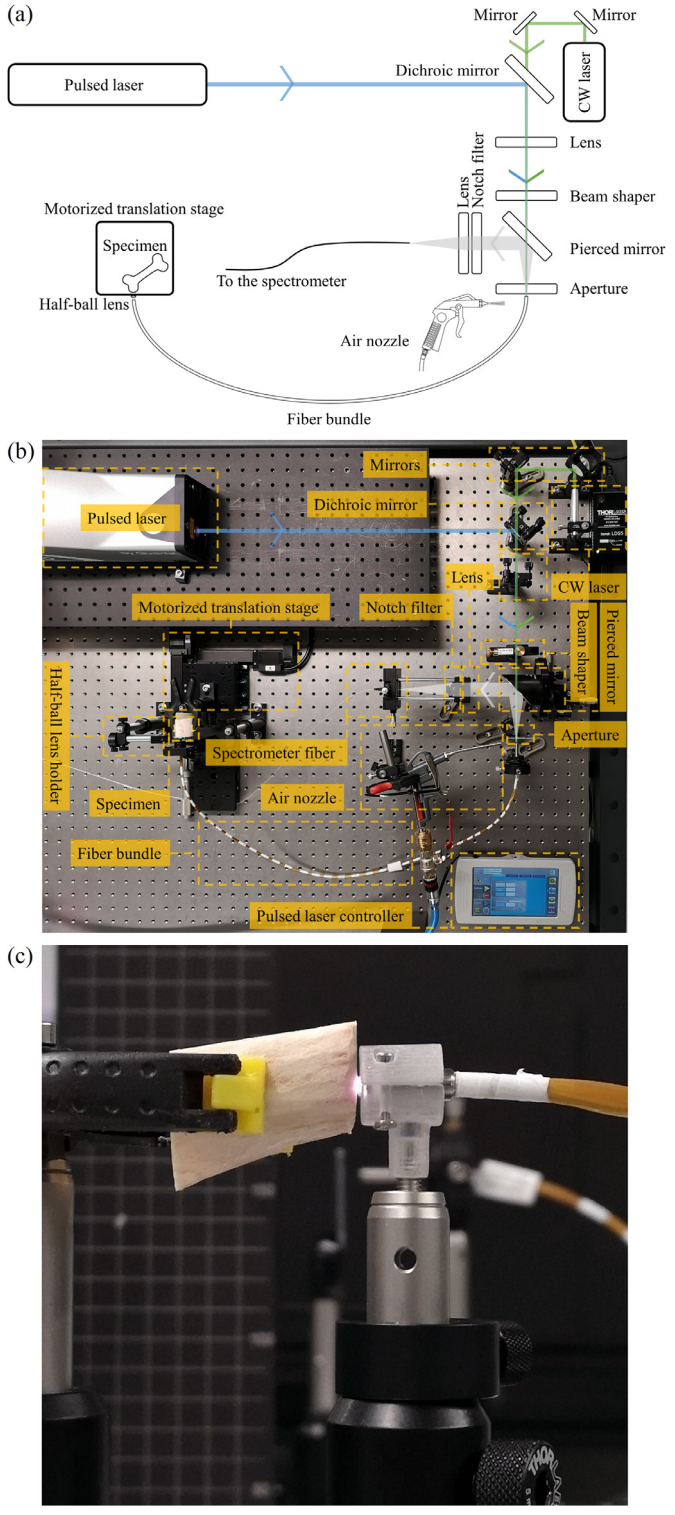


**Fig. 3.** (a) Schematic and (b) photograph of the experimental setup for laser beam delivery and plasma emission collection. The path of the pulsed laser, CW laser, and plasma emission are indicated by blue, green, and white lines, respectively. Arrows in (a) and (b) show the direction of light propagation. The half-ball lens (not marked in (a) and (b)) was clamped by a holder, 1.5 mm away from the fiber output. (c) Photograph of the bundle's tip.

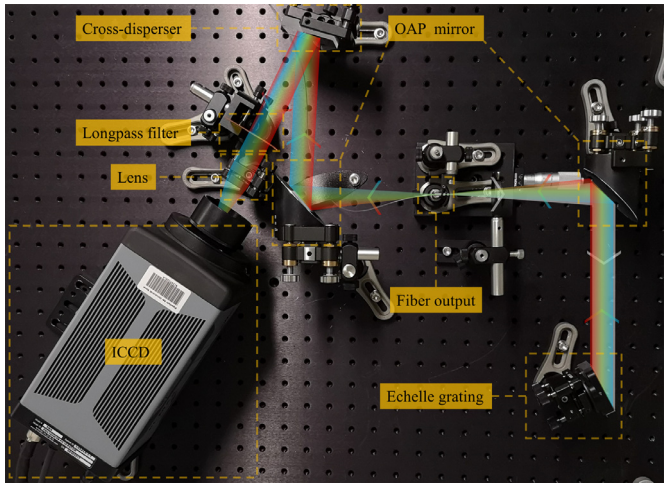


**Fig. 4.** Experimental setup of the customized Echelle spectrometer. The enclosure box has not been shown intentionally. The path of the light, from the fiber output to the detector, is highlighted. Arrows show the direction of light propagation.

The ICCD camera (PI-MAX 4, Princeton Instruments, USA) was synchronized with the laser Q-switched using TTL trigger pulses to have the proper time window for collecting plasma emission. The customized spectrometer was installed on top of a three-tier utility cart for portability. The middle tier was left empty for this study but could be used for a laser coupling system to achieve a portable LIBS setup. The bottom tier was dedicated to calibration instruments (a NIST traceable balanced Deuterium-Halogen light source for intensity calibration and some gas/vapor spectral lamps, including Mercury-Argon, Argon, Neon, and Krypton for wavelength calibration).

### 2.3. Specimen

Five bisected femora from porcine specimens (purchased from a local slaughterhouse) were used in this study. Each bisected tissue consisted of bone, bone marrow, fat, and muscle. From each side of each bisected specimen, 50 LIBS data points were collected from each tissue. In total, 2000 data points were collected (5 specimens × 4 tissue types × 2 sides × 50 shots).

### 2.4. Data analysis

The data collected from the five specimens were divided into five folds (each 400) to train a classifier in cross-validation (CV) mode. Afterward, each spectrum was normalized to its mean. Principal component analysis (PCA) was used to reduce data dimensionality while preserving as much of the data's variation as possible. The output of the PCA was used as input for a quadratic support vector machine (Q-SVM). An SVM with quadratic kernel was selected. It showed slightly better classification accuracy over other kernels. It was subsequently used to train a classifier on the training dataset and test the classifier on each fold's testing dataset. The data were analyzed using Matlab R2019b.

## 3. Results

Fig. 5 shows the Echellogram of the Deuterium-Halogen (DH) lamp. Fig. 6 shows the measured spectrum of four calibration lamps used for calibrating the spectrometer's wavelength.

The spectrometer's resolution was in the Angstrom range, sufficient for resolving peaks in the LIBS spectra (representing biological tissues) throughout the entire bandwidth. The spectrum of tissues is shown in Fig. 7.

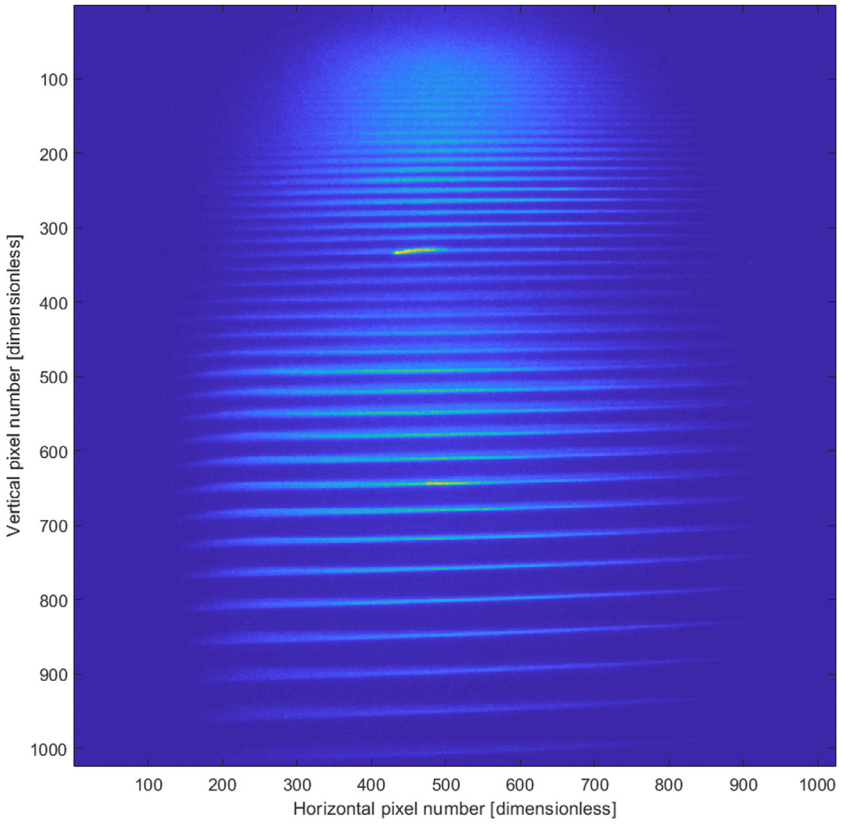


**Fig. 5.** Echellogram of Deuterium-Halogen (DH) lamp showing Echelle orders.

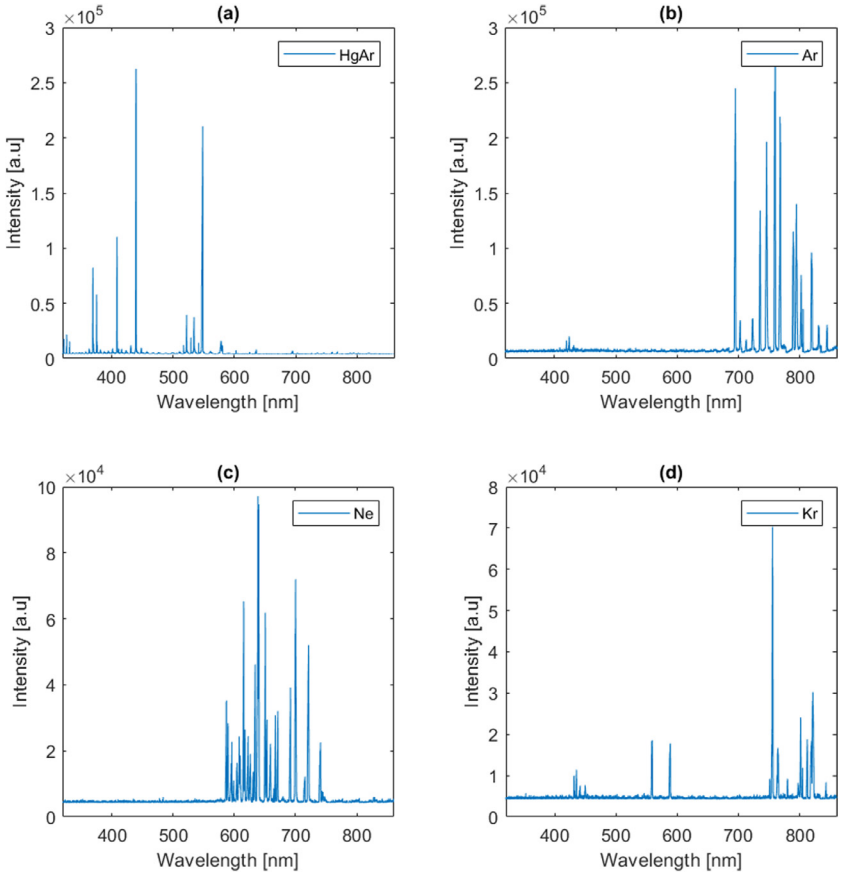


**Fig. 6.** The measured spectrum of calibration lamps used for calibrating the spectrometer's wavelength: (a) Mercury-Argon, (b) Argon, (c) Neon, and (d) Krypton.

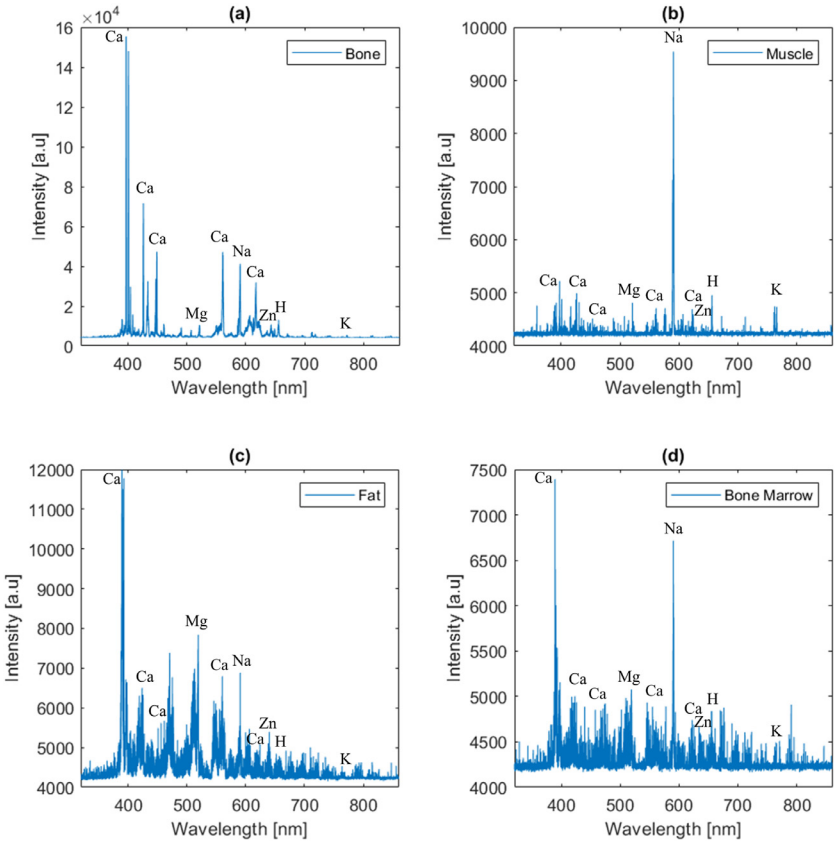


**Fig. 7.** LIBS spectrum of tissues: (a) bone, (b) muscle, (c) fat, and (d) bone marrow. The wavelength of some elements, including calcium (Ca), magnesium (Mg), sodium (Na), zinc (Zn), hydrogen (H), and potassium (K) are marked in each spectrum.

**Table 1**
Confusion matrix for the classifier.

| | Predicted class | | | | | | | |
|---|---|---|---|---|---|---|---|---|
| | Tissue | Bone | Muscle | Fat | Bone marrow | Sensitivity (CV) | Specificity (CV) | AUC |
| Actual class | Bone | 500 | 0 | 0 | 0 | 100% | 100% | 1.00 |
| | Muscle | 0 | 490 | 9 | 1 | 98% | 96.7% | 0.99 |
| | Fat | 0 | 20 | 423 | 57 | 84.6% | 94.1% | 0.96 |
| | Bone marrow | 0 | 30 | 79 | 391 | 78.2% | 96.1% | 0.95 |
| | | Average | | | | 90.2% | 96.7% | 0.98 |

After reducing the dimensionality of the data through PCA, the first six principal components (PCs) were used to feed the Q-SVM, which could classify bone from other soft tissues with 100% sensitivity and specificity (CV). The muscle was classified from other tissues with very high CV sensitivity (98%) and specificity (96.7%), as well. However, fat and bone marrow were classified with slightly lower CV sensitivity (84.6% and 78.2%) and specificity (94.1% and 96.1%).

Moreover, a receiver operating characteristic (ROC) curve was depicted and the area under the curve (AUC) was calculated (Fig. 8).

Table 1 shows the result of the classification.

## 4. Discussion

A few FO-LIBS systems had previously been proposed for biological tissue differentiation. However, endoscopic smart laser surgery systems require miniaturization and flexibility, as well. Therefore, a custom-made, bend-insensitive bundle delivery setup with sufficient flexibility was tested, in combination with a tiny half-ball lens at the bundle's tip (please see Section 2.1 for details of fiber delivery setup). The setup's dimensions and flexibility allowed for endoscopic application. Use of a bundle prevents self-focusing, as light does not penetrate between the individual fibers within the bundle. Compared to that of a single fiber, the larger cross-section of the bundle makes it less sensitive to mechanical movements (more robust setup), offering yet another benefit.

Due to the need to enhance sensitivity in an FO-LIBS setup, a custom-made Echelle spectrometer was developed and optimized for our application (please see Section 2.2 for details of the spectrometer design). We aimed to achieve the following specifications: 500 nm spectral bandwidth from 330 to 830 nm, at least 0.6 nm resolution, high optical throughput (low F-number), and compact size. Astigmatism aberrations in the spectrometer were minimized via off-axis parabolic mirrors. Coma aberrations were quelled by two collimators with an antiparallel configuration. Employing two collimators (first collimator in dual-pass mode) instead of one enabled us to maintain the Echelle grating in a quasi-Littrow configuration, with minimal deviation from the optical axis. Camera tilt compensated for longitudinal chromatic aberrations. Therefore, an appropriate resolving power was achieved within a sufficiently wide spectral bandwidth. Using off-axis mirrors eliminated the need for high focal-length designs. Therefore, we were able to keep the F-number of our design very low (i.e., 3). In the other designs, using a short focal-length necessitated tilting the mirror (producing extensive off-axis aberrations into the system). Mirrors with a 90° degree off-axis were used in this study because of their availability. However, a lower off-axis angle (e.g., 30°) would decrease aberrations in the system [47]. The compact size of the spectrometer made it portable. A portable

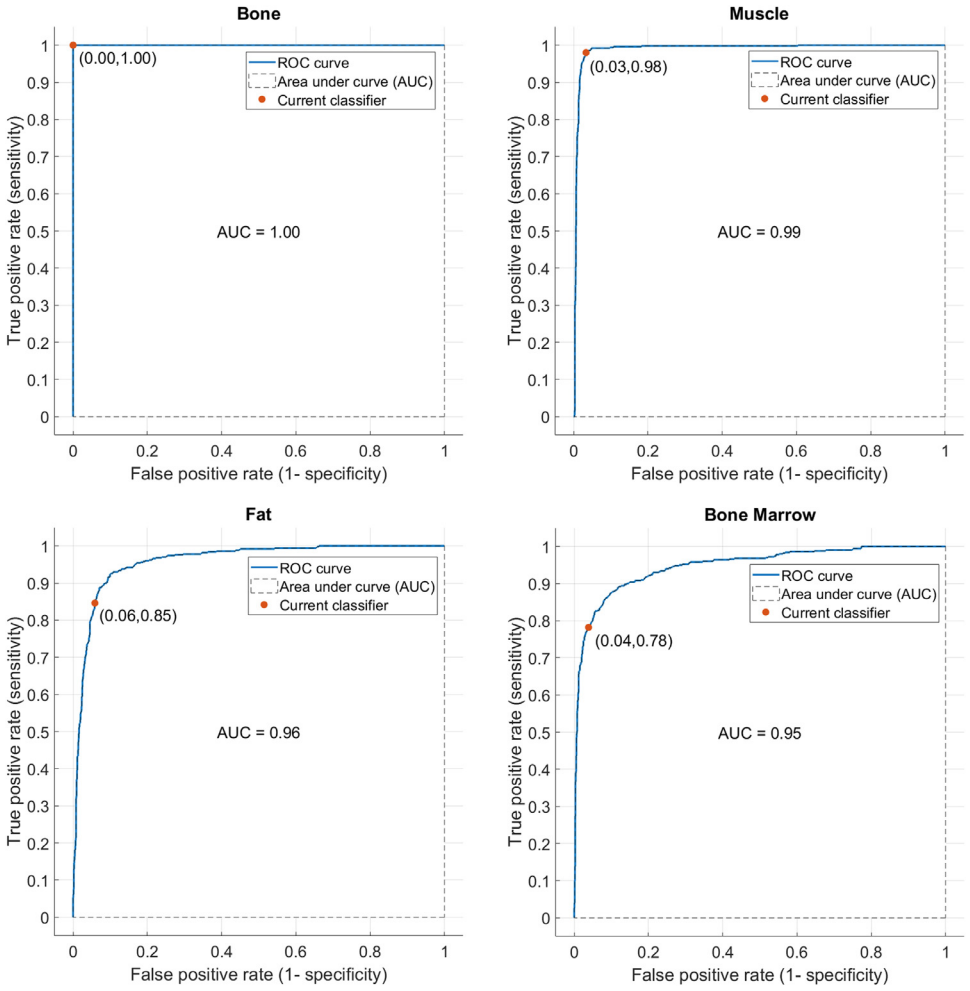


**Fig. 8.** ROC curve for the classifier for (a) bone, (b) muscle, (c) fat, and (d) bone marrow.

LIBS spectrometer is remarkably valuable for testing and characterizing different biological samples on-site. This is an excellent capability, especially if the target sample is potentially contagious. The customized LIBS setup was tested to differentiate bone from surrounding soft tissues, namely muscle, fat, and bone marrow. It is worth mentioning that since ablation is threshold-based, and plasma can initiate with lower energy in bone than in soft tissues [10], finding an optimum laser and ICCD parameter was challenging. For this study, the ICCD gate was open for 1 ms, after a 1 μs delay of the laser pulse, while the laser energy applied to specimens was 130 mJ. A higher intensity spectrum could be obtained with higher energies, but it leads to saturation of the ICCD's pixels while collecting the spectrum from the bone specimen. That is why in Fig. 7, the bone specimen yields a more intense signal than the soft tissues. The setup was able to differentiate bone from surrounding soft tissues (the requirement for endoscopic laserosteotomy) with 100% sensitivity and specificity (please see Section 2.3 and 2.4 for the details of the specimen and data analysis, respectively). The overall sensitivity and specificity for differentiating all tissues (the requirement for general endoscopic laser surgery) were 90.2% and 96.7%, respectively. The differentiation between fat and bone marrow accounts for most of the errors, as tissues have a similar chemical composition. An average classification error of 57.7% for differentiating bone marrow was reported after optoacoustic monitoring of Nd:YAG-laser-produced plasma using a Mach–Zehnder Interferometer [48]. However, averaging two subsequent data points might improve accuracy [49]. It should be noted that as bone marrow and fat are not adjacent tissues in the body, differentiating between them is less important than other tissues. The all-fiber-optic LIBS offers a stand-alone setup that does not need an additional laser for characterization, a common shortcoming of other miniaturized sensors developed for laser surgery monitoring [50].

## 5. Conclusion

The fiber delivery system proposed herein, including the bundle and the lens, was suitable for endoscopic application thanks to its small size and bend-insensitive flexibility. However, for successful endoscopic LIBS, a proper Echelle spectrometer was required as well. The main feature of most commercially available Echelle spectrometers is the ability to achieve the highest possible resolution and bandwidth at the same time. This meets the demand for a general device that is suitable for most applications. However, since optimizing all of the spectrometer parameters simultaneously is not possible, optical throughput is typically sacrificed to achieve simultaneous high-resolution and bandwidth. Low optical throughput reduces the system's sensitivity, so it does not work correctly in low light conditions (like those of miniaturized systems). The spectrometer was designed based on the spectral interval with most significant number of LIBS peaks for tissue differentiation (330 to 830 nm), and the resolution better than distance between the two closest peaks (0.6 nm) [24]. In our design, we reduced the bandwidth and resolution compared to the levels associated with commercially available Echelle spectrometers. Therefore, we were able to increase the optical throughput of the spectrometer. Our design leads to an F-number of 3, which is a significant improvement over other designs (typically ten or more). At the same time, we achieved the spectral bandwidth required to cover the essential biological LIBS peaks, and the resolution of the system exceeded the initial requirement. The

results show that the customized system was both sensitive and specific (selective) when differentiating tissues, label-free and in a single shot without sample preparation. The proposed setup is thus suitable for minimally-invasive smart laser surgery.

## Declaration of Competing Interest

The authors declare that they have no known competing financial interests or personal relationships that could have appeared to influence the work reported in this paper.

## CRediT authorship contribution statement

**Hamed Abbasi:** Conceptualization, Methodology, Software, Validation, Formal analysis, Investigation, Data curation, Writing – original draft, Writing – review & editing, Visualization. **Raphael Guzman:** Writing – review & editing, Supervision. **Philippe C. Cattin:** Writing – review & editing, Supervision, Funding acquisition. **Azhar Zam:** Conceptualization, Methodology, Resources, Writing – review & editing, Supervision, Project administration.

## Acknowledgement

The authors gratefully acknowledge funding from the Werner Siemens Foundation through the Minimally Invasive Robot-Assisted Computer-guided LaserosteotomE (MIRACLE) project. Moreover, the assistance given by Dr. Ferda Canbaz is highly appreciated.

## References

[1] Sotsuka Y, Nishimoto S, Tsumano T, Kawai K, Ishise H, Kakibuchi M, et al. The dawn of computer-assisted robotic osteotomy with ytterbium-doped fiber laser. Lasers Med Sci 2014;29:1125–9.
[2] Bernal LMB, Abbasi H, Zam A. Laser in Bone Surgery. In: Stübinger S, Klämpfl F, Schmidt M, Zeilhofer H, editors. Lasers in Oral and Maxillofacial Surgery. Springer; 2020. p. 99–109.
[3] Jowett N, Wöllmer W, Reimer R, Zustin J, Schumacher U, Wiseman PW, Mlynarek AM, Böttcher A, Dalchow CV, Lörincz BB. Bone ablation without thermal or acoustic mechanical injury via a novel picosecond infrared laser (PIRL). Otolaryngology–head and neck surgery 2014;150:385–93.
[4] Giraud JY, Villemin S, Darmana R, Cahuzac JP, Autefage A, Morucci JP. Bone cutting. Clin Phys Physiol Meas 1991;12:1–19.
[5] Pantawane M, Dahotre N. Challenges and advances in osteotomy. Ann Bone Joint Surg 2019;2(1):1007 2019.
[6] Dahotre NB, Joshi S. Machining of bone and hard tissues. Springer; 2016.
[7] Augello M, Deibel W, Nuss K, Cattin P, Jürgens P. Comparative microstructural analysis of bone osteotomies after cutting by computer-assisted robot-guided laser osteotome and piezoelectric osteotome: an in vivo animal study. Lasers Med Sci 2018;33:1471–8.
[8] Baek K-w, Dard M, Zeilhofer H-F, Cattin PC, Juergens P. Comparing the Bone Healing After Cold Ablation Robot-Guided Er:YAG Laser Osteotomy and Piezoelectric Osteotomy—A Pilot Study in a Minipig Mandible. Lasers Surg Med 2020.
[9] Stübinger S, Nuss K, Pongratz M, Price J, Sader R, Zeilhofer H-F, et al. Comparison of Er:YAG laser and piezoelectric osteotomy: An animal study in sheep. Lasers Surg Med 2010;42:743–51.
[10] Abbasi H, Beltrán Bernal LM, Hamidi A, Droneau A, Canbaz F, Guzman R, Jacques SL, Cattin PC, Zam A. Combined Nd:YAG and Er:YAG lasers for real-time closed-loop tissue-specific laser osteotomy. Biomedical Optics Express 2020;11:1790–807.
[11] Gaudiuso R, Melikechi N, Abdel-Salam ZA, Harith MA, Palleschi V, Motto-Ros V, et al. Laser-induced breakdown spectroscopy for human and animal health: A review. Spectrochim Acta, Part B 2019;152:123–48.
[12] Kasem MA, Gonzalez JJ, Russo RE, Harith MA. LIBS analysis of artificial calcified tissues matrices. Talanta 2013;108:53–8.
[13] Abdel-Salam ZA, Nanjing Z, Anglos D, Harith MA. Effect of experimental conditions on surface hardness measurements of calcified tissues via LIBS. Appl Phys B 2009;94:141–7.
[14] Abdel-Salam ZA, Galmed AH, Tognoni E, Harith MA. Estimation of calcified tissues hardness via calcium and magnesium ionic to atomic line intensity ratio in laser induced breakdown spectra. Spectrochim Acta, Part B 2007;62:1343–7.
[15] Abdel-Salam ZA, Palleschi V, Harith MA. Study of the feeding effect on recent and ancient bovine bones by nanoparticle-enhanced laser-induced breakdown spectroscopy and chemometrics. J Adv Res 2019;17:65–72.
[16] Kasem MA, Russo RE, Harith MA. Influence of biological degradation and environmental effects on the interpretation of archeological bone samples with laser-induced breakdown spectroscopy. J Anal At Spectrom 2011;26:1733–9.
[17] Tofanelli M, Pardini L, Borrini M, Bartoli F, Bacci A, D'Ulivo A, et al. Spectroscopic analysis of bones for forensic studies. Spectrochim Acta, Part B 2014;99:70–5.
[18] Kanawade R, Mehari F, Knipfer C, Rohde M, Tangermann-Gerk K, Schmidt M, et al. Pilot study of laser induced breakdown spectroscopy for tissue differentiation by monitoring the plume created during laser surgery — An approach on a feedback Laser control mechanism. Spectrochim Acta, Part B 2013;87:175–81.
[19] Mehari F, Rohde M, Knipfer C, Kanawade R, Klämpfl F, Adler W, Stelzle F, Schmidt M. Laser induced breakdown spectroscopy for bone and cartilage differentiation-ex vivo study as a prospect for a laser surgery feedback mechanism. Biomedical optics express 2014;5:4013–23.
[20] Kanawade R, Mahari F, Klämpfl F, Rohde M, Knipfer C, Tangermann-Gerk K, et al. Qualitative tissue differentiation by analysing the intensity ratios of atomic emission lines using laser induced breakdown spectroscopy (LIBS): prospects for a feedback mechanism for surgical laser systems. J Biophotonics 2015;8:153–61.
[21] Huang H, Yang L-M, Bai S, Liu J. Smart surgical tool. J Biomed Opt 2015;20:028001.
[22] Mehari F, Rohde M, Kanawade R, Knipfer C, Adler W, Klämpfl F, et al. Investigation of the differentiation of ex vivo nerve and fat tissues using laser-induced breakdown spectroscopy (LIBS): Prospects for tissue-specific laser surgery. J Biophotonics 2016;9:1021–32.
[23] Rohde M, Mehari F, Klämpfl F, Adler W, Neukam F-W, Schmidt M, et al. The differentiation of oral soft- and hard tissues using laser induced breakdown spectroscopy – a prospect for tissue specific laser surgery. J Biophotonics 2017;10:1250–61.
[24] Abbasi H, Rauter G, Guzman R, Cattin P, Zam A. Differentiation of femur bone from surrounding soft tissue using laser-induced breakdown spectroscopy as a feedback system for smart laserosteotomy. SPIE; 2018.
[25] Abbasi H, Rauter G, Guzman R, Cattin P, Zam A. Laser-induced breakdown spectroscopy as a potential tool for autocarbonization detection in laserosteotomy. J Biomed Opt 2018;23:071206.
[26] Abbasi H, Sugiarto I, Rauter G, Guzman R, Cattin P, Zam A. Pilot Ex Vivo Study of Laser-Induced Breakdown Spectroscopy to Detect Bone Dehydration: An Approach for Irrigation Feedback in Laserosteotomy. ICEECS; 2018.
[27] Abbasi H, Canbaz F, Guzman R, Cattin PC, Zam A. Highly flexible fiber delivery of a high peak power nanosecond Nd:YAG laser beam for flexiscopic applications. Biomedical Optics Express 2021;12:444–61.
[28] Bahreini M, Hosseinimakarem Z, Tavassoli SH. A study of association between fingernail elements and osteoporosis by laser-induced breakdown spectroscopy. J Appl Phys 2012;112:054701.
[29] Bahreini M, Ashrafkhani B, Tavassoli SH. Discrimination of patients with diabetes mellitus and healthy subjects based on laser-induced breakdown spectroscopy of their fingernails. J Biomed Opt 2013;18:107006.
[30] Bahreini M, Ashrafkhani B, Tavassoli SH. Elemental analysis of fingernail of alcoholic and doping subjects by laser-induced breakdown spectroscopy. Appl Phys B 2014;114:439–47.
[31] Gazmeh M, Bahreini M, Tavassoli SH. Discrimination of healthy and carious teeth using laser-induced breakdown spectroscopy and partial least square discriminant analysis. Appl. Opt. 2015;54:123–31.
[32] Henn K, Gubaidullin GG, Bongartz J, Wahrburg J, Roth H, Kunkel M. A spectroscopic approach to monitor the cut processing in pulsed laser osteotomy. Lasers Med Sci 2013;28:87–92.
[33] Abdel-Salam Z, Abdel-Salam SAM, Harith MA. Application of Laser Spectrochemical Analytical Techniques to Follow Up Spoilage of White Meat in Chicken. Food Anal Methods 2017;10:2365–72.
[34] Corsi M, Cristoforetti G, Giuffrida M, Hidalgo M, Legnaioli S, Palleschi V, Salvetti A, Tognoni E, Vallebona C. Analysis of biological tissues by laser induced breakdown spectroscopy technique. International Congress on Applications of Lasers & Electro-Optics 2003;2003:404.
[35] Corsi M, Cristoforetti G, Hidalgo M, Legnaioli S, Palleschi V, Salvetti A, Tognoni E, Vallebona C. Application of laser-induced breakdown spectroscopy technique to hair tissue mineral analysis. Appl. Opt. 2003;42:6133–7.
[36] Farsad M. A design cycle for echelle spectrometers. SPIE; 2017.
[37] Hoehse M, Mory D, Florek S, Weritz F, Gornushkin I, Panne U. A combined laser-induced breakdown and Raman spectroscopy Echelle system for elemental and molecular microanalysis. Spectrochim Acta, Part B 2009;64:1219–27.
[38] Sabsabi M, Detalle V, Harith MA, Tawfik W, Imam H. Comparative study of two new commercial echelle spectrometers equipped with intensified CCD for analysis of laser-induced breakdown spectroscopy. Appl. Opt. 2003;42:6094–8.
[39] Florek S, Haisch C, Okruss M, Becker-Ross H. A new, versatile echelle spectrometer relevant to laser induced plasma applications. Spectrochim Acta, Part B 2001;56:1027–34.
[40] Haisch C, Panne U, Niessner R. Combination of an intensified charge coupled device with an echelle spectrograph for analysis of colloidal material by laser–induced plasma spectroscopy. Spectrochim Acta, Part B 1998;53:1657–67.
[41] Iwai K, Takaku H, Miyagi M, Shi Y-W, Matsuura Y. Fabrication of Shatter-Proof Metal Hollow-Core Optical Fibers for Endoscopic Mid-Infrared Laser Applications. Fibers 2018;6:24.
[42] Sasazawa S, Kakino S, Matsuura Y. Optical-fiber-based laser-induced breakdown spectroscopy for detection of early caries. J Biomed Opt 2015;20:065002.
[43] Samek O, Telle HH, Beddows DCS. Laser-induced breakdown spectroscopy: a tool for real-time, in vitro and in vivo identification of carious teeth. BMC Oral Health 2001;1:1.
[44] Ahmadi M, Hassani RH, Kosa G, Zam A, Guzman R, Cattin PC, Rauter G. EndoCAT: An EtherCAT-based Articulated Rear View Endoscope for Single Port Surgery. In: 2018 7th IEEE International Conference on Biomedical Robotics and Biomechatronics (Biorob); 2018. p. 1070–5.
[45] Abbasi H, Rauter G, Guzman R, Cattin P, Zam A. Design and implementation of a compact high-throughput echelle spectrometer using off-the-shelf off-axis parabolic mirrors for analysis of biological samples by LIBS (Conference Presentation). SPIE; 2019.

[46] Abbasi H, Sahraei N, Canbaz F, Cattin PC, Zam A. Simulation of Echellogram Using Zemax OpticStudio and Matlab for LIBS. Cham: Springer International Publishing; 2021. p. 211–18.
[47] Probst RA, Steinmetz T, Wu Y, Grupp F, Udem T, Holzwarth R. A compact echelle spectrograph for characterization of astro-combs. Appl Phys B 2017;123:76.
[48] Kenhagho HN, Rauter G, Guzman R, Cattin PC, Zam A. Optoacoustic Tissue Differentiation Using a Mach–Zehnder Interferometer. IEEE Trans Ultrason Ferroelectr Freq Control 2019;66:1435–43.
[49] Nguendon Kenhagho H, Canbaz F, Gomez Alvarez-Arenas TE, Guzman R, Cattin P, Zam A. Machine Learning-Based Optoacoustic Tissue Classification Method for Laser Osteotomes Using an Air-Coupled Transducer. Lasers Surg Med 2020.
[50] Kenhagho HN, Canbaz F, Rauter G, Guzman R, Cattin P, Zam A. A First Approach to Miniaturized Optoacoustic Feedback Sensor for Smart Laser Osteotome : Fiber-Coupled Fabry-Pérot Etalon Sensor, 2019 2019:1–4.